ChemElectroChem

Research Article
doi.org/10.1002/celc.202200481

**Chemistry
Europe**
European Chemical
Societies Publishing

www.chemelectrochem.org

Special
Collection

Microkinetic Barriers of the Oxygen Evolution on the Oxides of Iridium, Ruthenium and their Binary Mixtures

Janis Geppert, Philipp Röse, Swantje Pauer, and Ulrike Krewer*[a]

The performance of electrocatalytic water splitting in polymer electrolyte membrane electrolysis is substantially determined by the microkinetic processes of the oxygen evolution reaction (OER). Even highly active catalysts such as the nanoparticulated transition metal oxides IrO_2, RuO_2 and their mixtures, $Ir_xRu_{1-x}O_2$, exhibit overpotentials up to several hundreds of millivolts. The surface of the oxide mixtures $Ir_xRu_{1-x}O_2$ is found to consist of actives sites of both Ir and Ru on which the OER mechanism is processed independently and at different overpotentials. By applying microkinetic modelling and parameterization via cyclic voltammograms we show that there is a correlation between performance and the relative Ir content, that can be explained by two different deprotonation steps. These are in particular the formation of the adsorbate species *OOH on rutile RuO_2 and *OO on IrO_2. The respective free reaction energies are quantified to 1.44 eV and 1.58 eV, which are the highest values of the process and thus determining the overpotential. The additional finding of adsorbed oxygen *O covering $>40\%$ of the active sites during the OER suggests that subsequent water adsorption is the major performance limiting step. Finally, a synergetic effect between both active sites on the binary transition metal oxides is identified: the respective other metal lowers the potential determining reaction energy on the Ru or Ir active site. This insight into the surface processes on Ir and Ru binary oxides forms the basis for deeper understanding of the active sites for further OER catalyst development.

Introduction

Electrocatalytic water splitting is a highly efficient reaction to convert sustainably generated excess electricity into chemical bonds as in molecular hydrogen.[1] In polymer electrolyte membrane electrolyzers, water is decomposed into oxygen and protons by the anodic oxygen evolution reaction (OER). The protons are reduced to hydrogen at the cathode in the so-called hydrogen evolution reaction. The latter is efficiently catalyzed with Pt-based materials,[2] whereas the OER requires a high overpotential even when using benchmark Ir-based catalyst. It is, therefore, the bottleneck reaction.[3] To increase the electrocatalytic activity of the OER and reduce the amount of the very scarce and, thus, expensive iridium, oxide mixtures containing various transition metals were investigated.[4] So far, the most promising catalyst results from the combination of Ir and Ru oxide, as it benefits from both, the high OER activity found for RuO_2 and the high stability of IrO_2.[5] Rutile-structured nanoparticles[6] as well as sputtered films[7] of $Ir_xRu_{1-x}O_2$ mixtures show increasing activity with higher Ru content, while electrocatalytic stability of nanoparticles is highest at a relative Ir content of 0.2 when an intermittent current is applied in acidic electrolyte.[6b]

The high electrocatalytic activity of single transition metal oxides is explained by complex catalytic processes: the overall OER $2H_2O \rightarrow 4H^+ + 4e^- + O_2$ is proceeding in multiple consecutive steps in which the catalyst surface provides active sites to form adsorbed but reactive intermediate species. According to density functional theory (DFT) studies on the OER on IrO_2[8] and RuO_2,[8a,9] several species such as *O, *OH and *OOH are thermodynamically favorable. They are produced by the adsorption of water and subsequent deprotonation.

To understand the overall performance of the electrocatalytic OER, it is crucial to quantify the kinetics of all reaction steps individually. This allows for analysis of the major process limitations in order to provide suggestions to further optimize the catalysts.

Thermodynamic binding energies of adsorbed OER intermediate species are reported for the single rutile structured transition metal oxides IrO_2 and RuO_2 and indicate the following process limitations: due to its high reaction energy, the formation of the *OOH species on the coordinately unsaturated site (CUS) of the (110) RuO_2 surface is reported to determine the potential of the overall process.[8a,10] In contrast, on the IrO_2 active site the reaction energy of the *OOH formation is significantly smaller and the subsequent deprotonation step is potential limiting as this step is thermodynamically less favorable.[8b,11] In our previous microkinetic modeling study, we further identified for the OER on rutile IrO_2 kinetic limitations by slow water adsorption on the *O species and the oxygen detachment,[11] which confirms DFT based findings.[12] Such

[a] *J. Geppert, Dr. P. Röse, S. Pauer, Prof. Dr.-Ing. U. Krewer*
Institute for Applied Materials – Electrochemical Technologies
Karlsruhe Institute of Technology
Adenauerring 20b, 76131 Karlsruhe, Germany
E-mail: ulrike.krewer@kit.edu

Special
Collection
This publication is part of a joint Special Collection with ChemCatChem on "Catalysts and Reactors under Dynamic Conditions for Energy Storage and Conversion (DynaKat)". Please check our homepage for more articles in the collection.

kinetic limitations have not yet been explicitly quantified for the RuO$_2$ material.

Despite the progress in the field, less effort was made to analyze the mechanism and kinetics on binary Iridium-Ruthenium oxide mixtures. It is known that they form well mixed bulk structures[13] as the bulk formation energy gets lowered.[14] The surface processes under OER conditions, however, are rarely studied. In a recent study of Reksten et al., lumped kinetic equations were derived for analyzing various options of limiting steps at combined Ir−Ru active sites.[15] By parameterizing the equations with experimental steady state polarization curves, the deprotonation of the *OH species was identified as rate limiting step.[15] Yet, further studies showed that good agreement with the experimental polarization data may be insufficient for a reliable kinetic identification. This was pointed out in microkinetic studies, in which different parameter sets and, thus, limiting steps were able to reproduce the same polarization curve of the general OER.[16] Also the assumption of a combined active site contradicts with DFT based findings of distinguishable Ru and Ir active sites. It was predicted that the CUS consists of either Ir or Ru surface atoms and that they show composition dependent binding energies for *O, *OH and *OOH adsorbed species.[14] This theory was recently supported by our experimental cyclic voltammetry (CV) measurements of deprotonation currents on the binary oxides, which are clearly assigned to either the pure RuO$_2$ or IrO$_2$.[6b] The finding of the Ir-content dependent binding energies[14] indicates that transferring the insights from the single transition metal oxides to binary mixtures might not be trivial. However, a significant influence on the OER performance can be expected. This impact of the material mixing on the kinetics of all individual steps in the OER mechanism on distinguishable Ir and Ru active surface sites was, to the best of our knowledge, never reported so far.

For a reliable identification of the kinetic surface processes, the use of dynamic analysis is suggested. It contains more information than analysis under steady state or quasi equilibrium assumptions, which may lead to multiple solutions, as discussed above.[16b] For dynamic analysis, a dynamic microkinetic modelling approach of the complex OER mechanism has shown to be a powerful tool to reproduce and study the interactions during a catalytic process.[11] In addition, the method allows to validate the model and its parameters with dynamic experimental data such as impedance spectroscopy[17] and CV measurements.[18]

Within this publication we determine and analyze the reaction kinetics and process interactions during the OER on rutile structured Ir−, Ru− and Ir$_x$Ru$_{1-x}$O$_2$ mixtures by employing a microkinetic model approach. A widely accepted OER mechanism from literature provides the basis to formulate the model equations. Parameterization is conducted by comparing the dynamic simulation results to experimental CV curves. With this, thermodynamic parameters such as the free reaction energies and free activation energies of individual process steps are quantified. We not only experimentally confirm theoretical findings on the single transition metal oxides IrO$_2$ and RuO$_2$ but also quantify and clarify the kinetics of individual process steps during the OER on binary Ir$_x$Ru$_{1-x}$O$_2$ mixtures. In a later section

we will give an in-depth understanding of the performance limiting reactions and identification of synergetic effects by material mixing.

Results and Discussion

In the following sections, we first present and discuss the microkinetics and thermodynamic energies for the single transition metal oxides RuO$_2$ and IrO$_2$. The results were gained from the model-based analysis method, which is in detail explained in the methodical section at the end of this paper. In short, the model equations were derived based on an OER mechanism gained from literature and shown in Scheme 1. The reaction rates were considered in forward and backward direction for all chemical and electrochemical processes at the active sites. This allows for dynamic simulations and the identification of the kinetic and thermodynamic properties by comparison to experimental CV curves. After the analysis of the single transition metal oxides, the microkinetics on Ir$_x$Ru$_{1-x}$O$_2$ mixtures will be reported and discussed in detail, as well as the effect of material mixing on the OER performance.

Kinetic Analysis of the OER at RuO$_2$ and IrO$_2$

For the following model-based analysis, high model validity is key to provide accurate and trustworthy results. With a three-step parameter estimation algorithm, which contains global and local optimization as well as a check for parameter identifiability, the main process defining parameter values were carefully quantified (see Computational Methods). Excellent agreement between the experimental CV results and the dynamic simulation data is shown for the OER on RuO$_2$ in Figure 1a and on IrO$_2$ in Figure 1b. The experimentally observed features for RuO$_2$ and IrO$_2$ are reproduced well by the models and both simulations show low root mean square errors (rmse) of 0.024 mA cm^{-2} and 0.069 mA cm^{-2}, respectively. Even when applying different potential scan rates, good reproducibility is achieved as shown in Figure S1 in the supporting information (SI). The high identifiability of the free reaction energy parameters is visible from rmse profile analysis shown in Figure S2 and in Figure S3 in the SI. In conclusion, a valid model
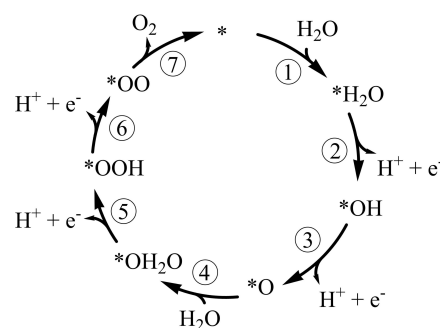
Scheme 1. Adsorbate evolution mechanism of the OER. The catalyst active site is denoted with asterisk *.[11]
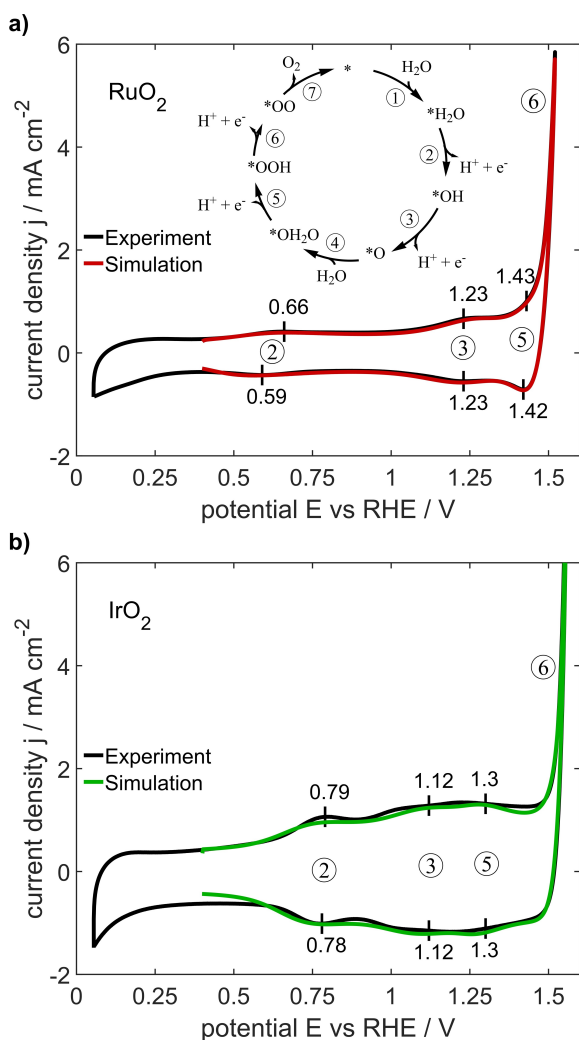
ChemElectroChem

Research Article
doi.org/10.1002/celc.202200481

Chemistry
Europe
European Chemical
Societies Publishing

Figure 1. Experimental and simulated CV curves a) on RuO_2 and b) on IrO_2 nanoparticulated catalysts in a 0.1 M H_2SO_4 solution at room temperature and a scan rate of 200 mV s^{-1}. Numbers in the figures correspond to the reaction steps of the reaction mechanism shown in the inset. The experimental data on RuO_2 was published previously.[6b]

with identified parameters is gained, which shows trustworthy results due to its excellent reproducibility of experimental data.

The assumed mechanism in Scheme 1 and the corresponding kinetics are thus a valid choice to reproduce the dynamic electrochemical behavior on both catalysts. To elucidate the kinetic limitations on RuO_2 and compare them to the kinetics on IrO_2, the seven reaction steps in Equations (1) to (7) can now be analyzed individually over a wide potential range. The sets of all estimated parameters for the reaction free energies, the activation free energies, the interaction free energies, the density of active sites and the double-layer capacitance are given in the SI. The values of the reaction free energy are normalized to electrochemical standard conditions, which are defined at room temperature and with the activities of all substances at unity. Note that, unless specified, the values are given at 0 V. At the lowest simulated potential of 0.4 V, water adsorption takes place:

$$* + H_2O \rightleftharpoons {}^*H_2O \tag{1}$$

The ratio between the free active site * and adsorbed water is defined by the reaction free reaction energy, which was quantified to $\Delta G^0_{r,1} = 0.24$ eV on RuO_2 and $\Delta G^0_{r,1} = 0.11$ eV on IrO_2. Water adsorption is, therefore, thermodynamically unfavorable, whereas kinetic simulation yields a water coverage of 10.4% on the RuO_2 surface and 34.8% on the IrO_2 surface. The high amount of free active sites on RuO_2 is also known from near ambient pressure X-ray photoelectron spectroscopy on RuO_2.[19] An increase in potential above 0.4 V starts the electrochemically driven deprotonation of adsorbed water, given in Equation (2).

$$^*H_2O \rightleftharpoons {}^*OH + H^+ + e^- \tag{2}$$

The reaction free energy values of $\Delta G^0_{r,2} = 0.51$ eV on RuO_2 and $\Delta G^0_{r,2} = 0.73$ eV on IrO_2 correlate with the potentials of the first redox transitions in Figure 1. Deviations from the noted potential values arise due to the preceding slow water adsorption. The small but notable value of the activation free energy for this process on RuO_2 of $\Delta G_{a,2} = 0.1$ eV is in good agreement with the shift in the absolute cathodic to anodic peak maxima observed in the experimental CV. On IrO_2, rather no shift is observed between cathodic and anodic absolute peak maxima of the experimental redox transition; this corresponds to an activation energy of $\Delta G_{a,2} = 0$ eV. Comparably low activation barriers of deprotonation steps were also reported in a DFT study, in which the authors explain this finding by the short traveling distance of the proton from the surface oxygen to the water molecule in the electrolyte.[20] A further increase in potential initiates the second deprotonation step, the deprotonation of *OH in Equation (3).

$$^*OH \rightleftharpoons {}^*O + H^+ + e^- \tag{3}$$

Mayor differences are observed in the potential and the reaction free energy parameters of this redox transition between both materials. On RuO_2, the process starts at a higher potential, which corresponds to a higher reaction free energy of $\Delta G^0_{r,3} = 1.28$ eV on RuO_2 than $\Delta G^0_{r,3} = 1.12$ eV on IrO_2. In comparison to DFT-based calculations,[21] our estimation for the reaction free energy on RuO_2 is in good accordance but the value on IrO_2 is slightly lower.

The subsequent step is the second water adsorption:

$$^*O + H_2O \rightleftharpoons {}^*OH_2O \tag{4}$$

On both catalysts, this chemical reaction requires high reaction energies of $\Delta G^0_{r,4} = 0.39$ eV on RuO_2 and $\Delta G^0_{r,4} = 0.54$ eV on IrO_2. This finding is qualitatively in good agreement with reported DFT results for RuO_2[22] and IrO_2.[12] This reaction energy does not only influence the lower potential region. It has also significant impact on the OER performance at potentials above 1.5 V. Figure 2a shows the free energies of all reaction steps on RuO_2 and IrO_2 corrected to the standard redox
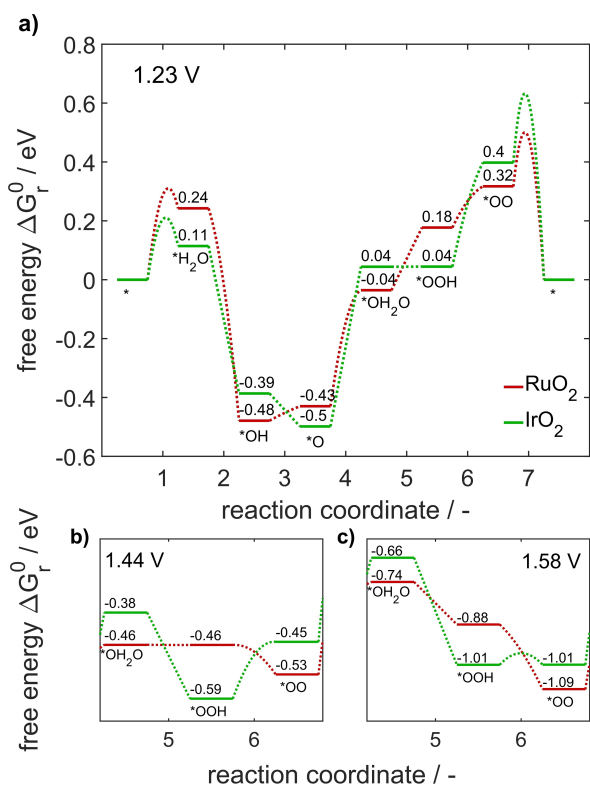
ChemElectroChem

Research Article
doi.org/10.1002/celc.202200481

**Chemistry
Europe**

European Chemical
Societies Publishing

Figure 2. Energy diagrams along the reaction coordinate of the OER mechanism given in Scheme 1 on RuO_2 (red) and on IrO_2 (green). The potential dependent reaction free energy values are denoted in full lines and the activation free energy barriers in dotted lines. Values are given at electrochemical standard conditions (room temperature and the activities of all substances at unity) and different potentials of a) 1.23 V, b) 1.44 V and c) 1.58 V.

potential of the OER of 1.23 V. It is clearly visible, that the second water adsorption in step 4 possesses the largest free energy of all steps. In consequence, this step limits the overall process chemically and is causing a high accumulation of the reactant species on the surface as shown in the SI in Figure S4 and Figure S5 on the Ru and the Ir active site, respectively. Adsorbed atomic oxygen, *O, is dominant even at the highest simulated potentials of 1.55 V and 1.6 V at which the OER is typically performed. This proves that chemical adsorption of water limits the overall OER rate. The third deprotonation step in Equation (5)

$$*OH_2O \rightleftharpoons *OOH + H^+ + e^- \qquad (5)$$

occurs on RuO_2 directly at the onset of the exponential increase of the OER, which has the overall highest value in reaction free energy of $\Delta G^0_{r,5} = 1.44$ eV. Hence, it is describing the potential determining step of the OER. As shown in the energy diagram in Figure 2b, an applied potential of 1.44 V is required to reach equilibrium conditions for this process step. On IrO_2 in contrast, the energy is lower with a value of $\Delta G^0_{r,5} = 1.23$ eV and, thus, the reaction takes place at potentials lower than the actual OER onset.

The reaction free energy of the fourth deprotonation step

$$*OOH \rightleftharpoons *OO + H^+ + e^- \qquad (6)$$

on RuO_2 $\Delta G^0_{r,6} = 1.37$ eV is smaller than the value from the previous step and is, thus, not the potential limiting step. However, on IrO_2 this step is crucial. With a reaction free energy value of $\Delta G^0_{r,6} = 1.58$ eV as the overall maximum, it represents the potential determining step. According to the energy diagram in Figure 2c, the thermodynamic equilibrium is reached at an applied potential of 1.58 V. The final step of the OER reaction mechanism marks the oxygen detachment given in Equation (7).

$$*OO \rightarrow * + O_2 \qquad (7)$$

The chemical process is thermodynamically favorable due to negative reaction free energies of $\Delta G^0_{r,7} = -0.32$ eV on RuO_2 and $\Delta G^0_{r,7} = -0.40$ eV on IrO_2, suggesting a fast reaction. Yet, the step is facing a strong kinetic barrier. In contrast to the previous reaction steps, very high activation free energies of $\Delta G_{a,7} = 0.34$ eV on RuO_2 and $\Delta G_{a,7} = 0.43$ eV on IrO_2 are quantified for the oxygen release, which is in qualitative agreement to DFT based findings on IrO_2 of $\Delta G_a = 0.58$ eV.[12] This activation barriers not only limit the overall OER process, but also lead to an accumulation of the reactant species *OO on the Ru and the Ir active site, as shown in the SI in Figure S4 and Figure S5, respectively.

In conclusion, the OER performance is constrained by three steps on each catalyst material: a chemical limitation by water adsorption on *O in Equation (4), the potential defining deprotonation of $*OH_2O$ on RuO_2 in Equation (5) and of *OOH on IrO_2 in Equation (6). Finally, a kinetic limitation of the oxygen detachment in Equation (7) is observed and explained by the high activation energy. Although the mechanism is identical on both materials, the catalytic activity is especially defined by the energy values of the respective potential determining steps. As those steps are different, we will analyze in the following, how the processes interact when mixing the materials.

Kinetic Analysis of the OER at Oxide Mixtures of $Ir_xRu_{1-x}O_2$

Binary mixtures of transition metal oxides may inherit characteristics from both materials. Ideally, this can lead to improved overall properties. For example, the binary mixtures of RuO_2 and IrO_2 provide lowered bulk formation energy[14] and are, thus, more stable than the pure RuO_2.[6b] They further show increased OER activity in comparison to the single metal oxide IrO_2.[6b] In the following, we will analyze the OER kinetics on $Ir_xRu_{1-x}O_2$ mixtures in order to understand the interactions and processes on the active sites and surface species, which lead to the observed increase in OER performance.

For the kinetic analysis of the binary transition metal oxides $Ir_xRu_{1-x}O_2$ we assume separate active sites consisting of Ru and Ir, as found by DFT calculations[14] and in dynamic CV experiments.[6b] In consequence, the OER mechanism including all the adsorption, desorption and deprotonation steps shown

ChemElectroChem

Research Article
doi.org/10.1002/celc.202200481

Chemistry
Europe
European Chemical
Societies Publishing

in Scheme 1 is assumed to proceed on both active sites independently. In a first step, the energy parameter values quantified for RuO_2 and IrO_2 were used and the relative Ir content x as well as the density of active sites were parameterized in order to minimize the deviation from experimental data. The experimental and simulated CV curves are given in the SI in Figure S6. A clear discrepancy between the experimental and simulated current density is observable between 1.3 V and 1.5 V. This results in deviations that are higher than for the single oxides and indicate, that the kinetics of at least one reaction step is not reproduced correctly by the parameters from the single oxides. Mixing the material causes, thus, interactions, which possibly have a synergetic effect of the activity and will be analyzed in the following.

To evaluate whether a change in energy parameters without modification of the OER mechanism allows to properly describe the experimental observed behavior of the mixtures, the parameters were newly identified by using the parameters from RuO_2 and IrO_2 as initial values for the Ru and Ir active sites, respectively. The assumption of different energy values is in full agreement with DFT calculations, which suggested a change in binding energy of adsorbed species with different relative Ir content.[14] Also the density of active sites, the double-layer capacitance and the relative content of Ir active sites was identified. A change in the relative Ir content of the surface composition was considered to account for possible deviations between the nominal bulk and the surface.[6b] The parameter sets as well as the rmse profile are given in the SI. The resulting simulated CV curves in Figure 3 show an excellent agreement with the experimental CV curves for all three binary catalyst mixtures. This confirms that the mechanism still holds, but that there exist energetic interactions for the mixtures.

The analysis of the free energy values and the changes of surface coverages with potential in Figure S4 and Figure S5 in the SI reveals similar process limitations for all mixtures as for the previously discussed single oxides: On both Ir and Ru active sites, the water adsorption step in Equation (4) shows limiting behavior. Also, the oxygen detachment step of Equation (7) faces a high, thus kinetically limiting, activation energy. The highest reaction free energy on the Ir active site is obtained for

the deprotonation of *OOH in Equation (6) for all mixtures. And the highest reaction free energy on the Ru active site is identified for the deprotonation of $*OH_2O$, Equation (5), for all mixtures with high Ru-content, i.e., $Ir_{0.2}Ru_{0.8}O_2$ and $Ir_{0.5}Ru_{0.5}O_2$. In contrast, for $Ir_{0.8}Ru_{0.2}O_2$, deprotonation energy of $*OH_2O$ gets lower and the deprotonation of *OOH becomes limiting, similar to the Ir-sites. Since the highest reaction free energy on the Ru active site is lower compared to the value on the Ir site, the mentioned steps on the Ru active site are determining the overall potential.

We will now analyze the contribution of Ru and Ir sites to the performance of the CV. At $Ir_{0.2}Ru_{0.8}O_2$, the current density shown in Figure 3a is strongly impacted by deprotonation on both, Ru and Ir active sites. The single processes at Ir and Ru sites occur at similar potentials as on the discussed single oxides; as the potentials differ between RuO_2 and IrO_2, redox transitions at Ir and Ru sites can be distinguished. The large share of Ir to the current in the CV can be explained as follows: Although the nominal relative bulk Ir content is 0.2, the identified relative active site content at the surface is twice this value, with a share of 0.4. Thus, the Ir signal contributes much more than 20% to the CV curves at potentials below OER. Indeed, a similar accumulated Ir content on the surface was also experimentally found by conducting X-ray photoelectron spectroscopy (XPS) and was explained by the comparably fast dissolution of Ru species in acidic electrolyte.[5a,6b] The experimental values in Figure 4 are in good accordance with the model results. The accumulation of Ir at the surface can also be seen in the experimental and simulation data of $Ir_{0.5}Ru_{0.5}O_2$ and less pronounced in the data of $Ir_{0.8}Ru_{0.2}O_2$. Finally, it is interesting to see for $Ir_{0.2}Ru_{0.8}O_2$ a notable difference between current shares in the CV between the adsorption region and the OER region. Whereas currents in the adsorption region below 1.5 V are equally strong on both active sites, the turnover frequency of the OER is mainly defined by the processes at the Ru active sites: Ru sites convert more than two third of the electrons at the highest simulated potential of 1.55 V. Thus, Ru sites are more active during the OER.

In Figure 3b, the experimental and simulated cyclic voltammograms of $Ir_{0.5}Ru_{0.5}O_2$ are shown. At potentials prior to the

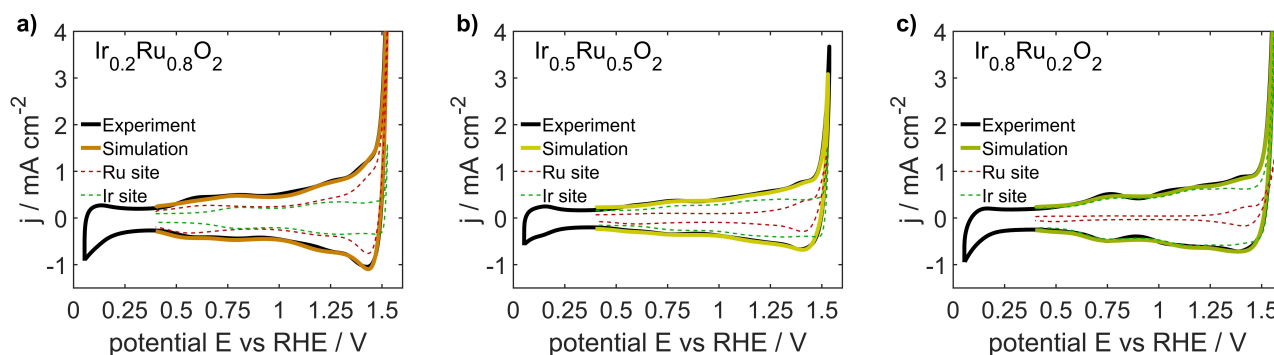**Figure 3.** Experimental and simulated cyclic voltammetry curves on the binary oxides a) $Ir_{0.2}Ru_{0.8}O_2$, b) $Ir_{0.5}Ru_{0.5}O_2$ and c) $Ir_{0.8}Ru_{0.2}O_2$, with rmse values of 0.033 mA cm^{-2}, 0.017 mA cm^{-2} and 0.032 mA cm^{-2}, respectively. The simulations allow to distinguish between the processes at the Ru and Ir active sites, which results in the current densities given with the dotted red and green lines, respectively. The data was recorded at 200 mV s^{-1} in 0.1 M H_2SO_4 solution at room temperature. The experimental data on $Ir_{0.2}Ru_{0.8}O_2$ and $Ir_{0.5}Ru_{0.5}O_2$ was published previously.[6b]

ChemElectroChem

Research Article
doi.org/10.1002/celc.202200481

Chemistry Europe
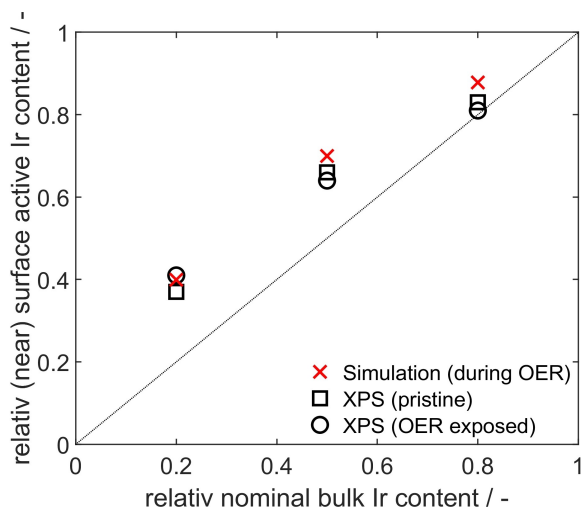European Chemical
Societies Publishing

Figure 4. Model-based estimation and XPS-measured values of the relative content of Ir active sites on the surface in comparison to the nominal bulk content. The experimental data was published previously.[6b]
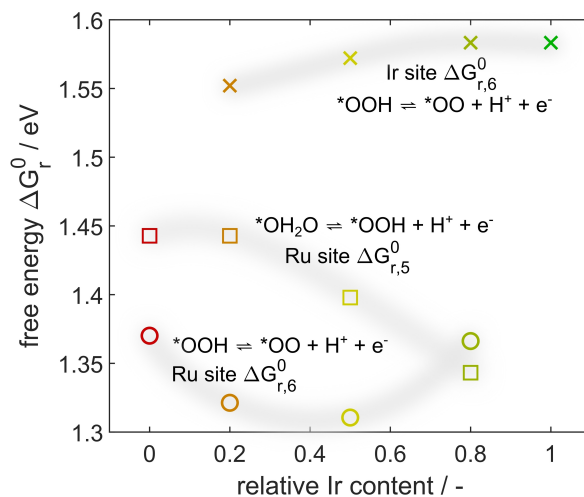

Figure 5. Reaction free energy values identified for the potential determining deprotonation steps of the OER on the Ru active site (circle, square) and the Ir active site (x) of RuO_2, IrO_2 and the $Ir_xRu_{1-x}O_2$ mixtures with respect to the nominal relative content of bulk Ir.

oxygen evolution, the main current contribution arises from the deprotonation processes on the Ir active site. Also, here the identified share of active Ir sites on the catalyst surface is 0.7 and thus higher than the bulk value. This observation corresponds to the XPS-measured relative surface Ir content of the same material.[6b] As a result, the contribution of the processes on Ir to the overall current in the CV is much higher than at $Ir_{0.2}Ru_{0.8}O_2$. At the OER potential of 1.55 V, the number of electrons, which are transferred at all active Ir and Ru sites are roughly the same. This seemingly contradicts thermodynamic expectations, as the reaction energy of the potential determining step on Ir sites, $\Delta G^0_{r,6} = 1.57$ eV, is higher than on the Ru site with $\Delta G^0_{r,5} = 1.40$ eV. Yet, it can be well explained by the increased Ir site content and the kinetics, as the share of the surface covered by reactant species differs from of $\theta_{Ru,OH2O} < 0.01$ on the Ru site to $\theta_{Ir,OOH} = 0.17$ on the Ir site. Thus, the potential determining step on the Ru site is decelerated due to the low amount of both the reactant species and the active sites.

Finally, the CV curves of the $Ir_{0.8}Ru_{0.2}O_2$ binary oxide and the corresponding partial current densities are given in Figure 3c. They show dominating processes at the Ir site over the full potential range due to the fact, that the estimated share of Ir active sites given in Figure 4 is 0.88. Nevertheless, as the OER processes at 1.55 V, the Ru site still contributes roughly 20% of the total current density. Thus, the turn over frequency per active site is still higher on the Ru site, then on the Ir site.

Having discussed the partial currents in the CV curves on the Ir and Ru active sites, we will now elucidate the synergetic effect of material mixing on the potential determining OER steps. An overview of the changes in reaction free energies, which essentially determine the activity of the IrO_2, RuO_2 and their mixed oxides is shown in Figure 5. As previously explained, for Ir-contents until 50%, the potential determining step of OER on the Ru active site is the deprotonation step $*OH_2O \rightleftharpoons *OOH + H^+ + e^-$ given in Equation (5). In contrast, on the Ir active site

the deprotonation step $*OOH \rightleftharpoons *OO + H^+ + e^-$ in Equation (6) was identified as potential determining step of the reaction. For the energy values, there is a clear trend that applies for both sites: as the content of the dominant active site decreases, the reaction free energy of this site is lowered. Thus, the mixed oxides exhibit a synergetic effect that results in higher OER activity at both individual active sites. On the Ru site this effect is strongest for the mixed oxides with a relative Ir content of 0.8. On this material the reaction free energy $\Delta G^0_{r,5} = 1.34$ eV of the step in Equation (5) is lowered and undercuts the reaction free energy $\Delta G^0_{r,6} = 1.37$ eV of the subsequent process in Equation (6). This results in *OOH deprotonation becoming the potential determining step on Ru for high Ir contents. Despite the fact of a lowered share of active Ru sites present at the surface, the synergies promoted by the material structure provide overall improved kinetics at both active sites.

This work clearly shows that while the same mechanism holds for the single transition metal oxides and the binary mixtures, the material mixing leads to a decrease in reaction free energies of the potential determining steps and, thus, improved OER performance at both active sites. As the reaction free energies are directly related to the binding energy of adsorbed species, we show that these can be tuned by adding other atoms in such way that higher catalytic activity is achieved. While $Ir_xRu_{1-x}O_2$ is also commercially attractive, it serves as a well characterized material to study the origin of this effect and a possible correlation to the electronic band structure, to gain an in-depth understanding of the active catalyst material. Ir mixing with other materials than Ru lowers the cost and might also provide an increased activity of the Ir active sites. This prediction might be especially useful for future studies, which are aiming for further catalyst development.

ChemElectroChem

Research Article
doi.org/10.1002/celc.202200481

Chemistry Europe
European Chemical
Societies Publishing

Conclusion

In the presented work we provided an in-depth kinetic analysis of the reactions and adsorption processes and their limitations on Ir and Ru active sites during the OER via a microkinetic model. The kinetic model and the underlying mechanism allow to reproduce CV curves of IrO_2, RuO_2 and their binary mixtures $Ir_xRu_{1-x}O_2$. The surface of the binary mixed oxides $Ir_xRu_{1-x}O_2$ show an accumulation of Ir active sites, which exceeds that of the bulk stoichiometry and is in accordance with recent experimental studies. Major findings are that two chemical steps, which are the water adsorption ($*O \rightleftharpoons *OH_2O$) and the oxygen release ($*OO \rightarrow * + O_2$) significantly impact the OER on all catalysts. Further, two different deprotonation steps, depending on whether the active site consists of Ru ($*OH_2O \rightleftharpoons *OOH + H^+ + e^-$) or Ir ($*OOH \rightleftharpoons *OO + H^+ + e^-$) determine the OER potential at which the OER is conducted. We reveal that the surface processes of the OER are taking place on both, the Ru and the Ir active site, individually, by a quantification of both corresponding current densities. Yet, a positive synergetic impact on the electrocatalytic activity by mixing the materials is revealed: the thermodynamic reaction free energies of the potential determining steps are lowered for the processes on both the Ru and the Ir active sites. In consequence, not only the presence of the highly active Ru sites provides increased performance but also the compositional change leads to better Ir site activity. This effect might have a beneficial impact in further mixed oxide catalyst development.

Experimental Section

To parameterize the microkinetic model, a proper experimental dataset is required. The experimental current densities from the CV data used for this analysis were already published for the pure oxides and the mixtures by Escalera-López et al.[6b] CV curves of IrO_2 and $Ir_{0.8}Ru_{0.2}O_2$ were remeasured with the same method but with a higher applied maximum potential of up to 1.6 V vs RHE to guarantee for a full exploitation of the OER behavior. We here briefly summarize the experimental method: Flame spray pyrolyzed nanoparticles were calcined at 600 °C, which results in rutile structured single crystals. 2 mg of the material was mixed with 750 µL of deionized water, 250 µL of isopropanol 8.58 µL of Nafion 5% dispersion (D-520, VWR) and 1.2 µL of 1 M KOH. 10 µL of the resulting ink was drop casted onto in a glassy carbon working electrode with a geometric area of $A = 0.1963 \text{ cm}^2$. The electrode with the pristine particles was put into the PTFE cell filled with 0.1 M H_2SO_4 electrolyte solution together with a Pt wire as counter electrode and a HydroFlex reversible hydrogen electrode from Gaskatel GmbH. Using a Gamry Reference 600+ potentiostat, impedance spectroscopy measurements at open circuit potential with frequencies from $f = 10^{-1}$ to $f = 10^5$ Hz and a perturbation amplitude of $E = 10$ mV as well as three consecutive CV curves in between potentials of $E = 0.05$ and 1.6 V were recorded with a potential rate of $dE/dt = 200 \text{ mV s}^{-1}$. The potential was corrected afterwards by the Ohmic resistance gained from the impedance spectroscopy analysis. The consideration of data over such a wide potential range is important due to the fact that the faradaic current of only the OER itself provides little information for parameter identification as multiple processes contributing here to the overall current simultaneously.[16b] Aiming for a better process

discrimination, the careful analysis of the potential region prior to the OER allows to gain essential kinetic information about of the reactions proceeding here as well.

Computational Methods

The microkinetic simulations were conducted with a model implemented in the software MATLAB 2020b. The procedure follows that of our prior work.[11] In the following section, we provide the assumptions and main equations of the model as well as the parameterization process.

For modelling the processes at the catalytic surface, we assume the adsorbate evolving mechanism to take place, as it is widely agreed on in literature for IrO_2,[8b,11] RuO_2[10] and even for their mixtures.[14–15] It is shown in Scheme 1 and consists of water adsorbing on the active site, denoted with *, in steps (1) and (4), producing $*H_2O$ and $*OH_2O$, respectively. Via deprotonation in steps (2), (3), (5), and (6), several respective intermediate species *OH, *O, *OOH and *OO are formed, and adsorbed OO is detached in step (7), resulting in the final product of molecular oxygen.

To simulate the dynamic changes during a CV, a time t dependent potential E is set in Equation (8)

$$E(t) = E_0 + t\frac{dE}{dt} - j(t)AR \tag{8}$$

With a starting potential E_0 and a constant potential rate dE/dt to reproduce the experimentally applied potential. The experimental potential drop in the electrolyte is corrected by subtracting its measure calculated by multiplying the current density j, the geometric electrode area A and the electrolyte resistance R. The reaction rates r_i of the single steps $i \in \{1, 2, 3 \ldots 7\}$ according to Scheme 1 are calculated in Equation (9) and (10) for forward direction r_{+i} and for backward directions r_{-i}, respectively.

$$r_{+i} = \prod_j \left(a_j^{v_{+ij}} \cdot \theta_j^{v_{+ij}} \right) f_{+i}(\theta) k_0 \cdot$$
$$\exp\left(\frac{-\Delta G_{a,i} - \beta \Delta G_{r,i} + \beta |v_{ie^-}| eE}{k_B T} \right), \forall j \in \Omega, \forall i \tag{9}$$

$$r_{-i} = \prod_j \left(a_j^{v_{-ij}} \cdot \theta_j^{v_{-ij}} \right) f_{-i}(\theta) k_0 \cdot$$
$$\exp\left(\frac{-\Delta G_{a,i} + \beta \Delta G_{r,i} - \beta |v_{ie^-}| eE}{k_B T} \right), \forall j \in \Omega, \forall i \tag{10}$$

The surface coverage θ_j by void or adsorbed species $j \in \Omega_{sur} = \{*; *H_2O; *OH; *O; *OH_2O; *OOH; *OO\}$ are defined to sum up to unity $x \cdot \sum \theta_j^{Ir} + (1-x) \cdot \sum \theta_j^{Ru} = 1$, and the activities a_j of all electrolyte species $j \in \Omega_{el} = \{H^+; H_2O; O_2\}$ are set constant as given by the experimental conditions. The matrix of the stoichiometric coefficients v of the adsorbed species, the electrolyte species and the transferred electrons are derived from the mechanism in Scheme 1 in forward v_+ and backward direction v_-. The differences in binding energies of the product and the reactant species of each reaction i are defined as the reaction free energies $\Delta G_{r,i}$. Additional kinetic energy barriers in both directions alongside the reaction coordinate are considered by the activation free energy $\Delta G_{a,i}$. Further, the temperature T, the Boltzmann constant k_B, the elementary charge e and the symmetry factor β are implemented. The preexponential frequency factor k_0 is set to a constant value for all reactions to avoid over-parameterization, as the experimental data does not allow to determine the frequency factor and the free activation

ChemElectroChem

Research Article
doi.org/10.1002/celc.202200481

Chemistry Europe
European Chemical
Societies Publishing

energy independently.[23] We consider additional effects on the energy level of species through areal spacing of the surface sites and the interaction of adsorbed species $\Delta G_{\mathrm{int},j}$. For this, we implement the van der Waals adsorption isotherm or also called Hill-de-Boer isotherm. As described elsewhere,[18a,24] the isotherm is adapted to the model in the form of a function $f_i(\theta), \forall\, j \in \Omega_{\mathrm{sur}}, \forall\, i$ for forward and backward direction in Equation (11) and (12), respectively.

$$f_{+i}(\theta) = \exp\left(\beta\left[\prod_j\left(\frac{\Delta G_{\mathrm{int},j}}{k_BT}\theta_j\right)^{\nu_{+ij}} - \prod_j\left(\frac{\Delta G_{\mathrm{int},j}}{k_BT}\theta_j\right)^{\nu_{-ij}} + \prod_j\frac{\theta_j^{\nu_{+ij}}}{\theta_j^{\nu_{-ij}}} - \prod_j\frac{\theta_j^{\nu_{-ij}}}{\theta_j^{\nu_{+ij}}}\right]\right) \quad (11)$$

$$f_{-i}(\theta) = \exp\left(\beta\left[\prod_j\left(\frac{\Delta G_{\mathrm{int},j}}{k_BT}\theta_j\right)^{\nu_{-ij}} - \prod_j\left(\frac{\Delta G_{\mathrm{int},j}}{k_BT}\theta_j\right)^{\nu_{+ij}} + \prod_j\frac{\theta_j^{\nu_{-ij}}}{\theta_j^{\nu_{+ij}}} - \prod_j\frac{\theta_j^{\nu_{+ij}}}{\theta_j^{\nu_{-ij}}}\right]\right) \quad (12)$$

The balance of all species covering the surface is given in Equation (13).

$$\frac{d\theta_j}{dt} = \sum_i \nu_{ij}\cdot(r_{+i} - r_{-i}), \;\; \forall\, j \in \Omega_{\mathrm{sur}} \quad (13)$$

The balance of charge q in Equation (14) allows to calculate the current density and, hence, to solve the set of equations dynamically. This equation accounts for the charge accumulated in the double layer of the catalyst with its capacitance C_{dl} and the sum of sinks and sources due to the electrochemical reactions by taking the Faraday constant F and the density of active sites ρ with respect to the geometric electrode area into account.

$$\frac{dq}{dt} = C_{\mathrm{dl}}\cdot\frac{dE}{dt} = j(t) - F\rho\sum_i \nu_{\mathrm{ie}^-}\cdot(r_{+i} - r_{-i}), \;\; \forall\, i \quad (14)$$

The resulting current density j of a cyclically applied potential is compared to experimental current j_{exp} during the CV with the aim to estimate the model parameters, which are the free energies, the density of active sites and the double-layer capacitance. For best estimation, the root mean squared error (rmse) in Equation (15)

$$rmse = \sqrt{\frac{1}{N}\sum_n (j - j_{\mathrm{exp}})^2} \quad (15)$$

is minimized by two optimization algorithms: 10^6 sets of randomly defined parameter values are simulated. The 20 sets of parameters resulting in the lowest rmse are further optimized by the MATLAB build-in pattern search algorithm, each with a total of 98,000 objective function iterations. For the reaction free energy parameters of the single transition metal oxides RuO_2 and IrO_2, a profile rmse analysis with deviations of {(−0.2); −0.1; −0.05; 0; 0.05; 0.1; (0.2)} eV was conducted with 25,000 objective function iterations. This is used in the same way as the profile likelihood method is used to check for parameter identifiability.[25]

Acknowledgements

Conflict of Interest

The authors declare no conflict of interest.

Data Availability Statement

The data that support the findings of this study are available from the corresponding author upon reasonable request.

[1] K. F. Kalz, R. Kraehnert, M. Dvoyashkin, R. Dittmeyer, R. Glaser, U. Krewer, K. Reuter, J. D. Grunwaldt, *ChemCatChem* **2017**, *9*, 17–29.

[2] J. N. Hansen, H. Prats, K. K. Toudahl, N. Morch Secher, K. Chan, J. Kibsgaard, I. Chorkendorff, *ACS Energy Lett.* **2021**, *6*, 1175–1180.

[3] M. Bernt, H. A. Gasteiger, *J. Electrochem. Soc.* **2016**, *163*, F3179–F3189.

[4] a) Z. Shi, X. Wang, J. Ge, C. Liu, W. Xing, *Nanoscale* **2020**, *12*, 13249–13275; b) M. Carmo, D. L. Fritz, J. Mergel, D. Stolten, *Int. J. Hydrogen Energy* **2013**, *38*, 4901–4934; c) K. Zhang, R. Zou, *Small* **2021**, *17*, e2100129; d) I. C. Man, H. Y. Su, F. Calle-Vallejo, H. A. Hansen, J. I. Martínez, N. G. Inoglu, J. Kitchin, T. F. Jaramillo, J. K. Nørskov, J. Rossmeisl, *ChemCatChem* **2011**, *3*, 1159–1165.

[5] a) S. Cherevko, S. Geiger, O. Kasian, N. Kulyk, J.-P. Grote, A. Savan, B. R. Shrestha, S. Merzlikin, B. Breitbach, A. Ludwig, K. J. J. Mayrhofer, *Catal. Today* **2016**, *262*, 170–180; b) O. Kasian, S. Geiger, P. Stock, G. Polymeros, B. Breitbach, A. Savan, A. Ludwig, S. Cherevko, K. J. J. Mayrhofer, *J. Electrochem. Soc.* **2016**, *163*, F3099–F3104.

[6] a) J. Cheng, H. Zhang, G. Chen, Y. Zhang, *Electrochim. Acta* **2009**, *54*, 6250–6256; b) D. Escalera-López, S. Czioska, J. Geppert, A. Boubnov, P. Röse, E. Saraçi, U. Krewer, J.-D. Grunwaldt, S. Cherevko, *ACS Catal.* **2021**, *11*, 9300–9316.

[7] R. Kötz, S. Stucki, *Electrochim. Acta* **1986**, *31*, 1311–1316.

[8] a) J. Rossmeisl, Z. W. Qu, H. Zhu, G. J. Kroes, J. K. Nørskov, *J. Electroanal. Chem.* **2007**, *607*, 83–89; b) Y. Ping, R. J. Nielsen, W. A. Goddard 3rd, *J. Am. Chem. Soc.* **2017**, *139*, 149–155.

[9] R. R. Rao, M. J. Kolb, L. Giordano, A. F. Pedersen, Y. Katayama, J. Hwang, A. Mehta, H. You, J. R. Lunger, H. Zhou, N. B. Halck, T. Vegge, I. Chorkendorff, I. E. L. Stephens, Y. Shao-Horn, *Nat. Catal.* **2020**, *3*, 516–525.

[10] R. R. Rao, M. J. Kolb, N. B. Halck, A. F. Pedersen, A. Mehta, H. You, K. A. Stoerzinger, Z. Feng, H. A. Hansen, H. Zhou, L. Giordano, J. Rossmeisl, T. Vegge, I. Chorkendorff, I. E. L. Stephens, Y. Shao-Horn, *Energy Environ. Sci.* **2017**, *10*, 2626–2637.

[11] J. Geppert, P. Röse, S. Czioska, D. Escalera-López, A. Boubnov, E. Saraçi, S. Cherevko, J.-D. Grunwaldt, U. Krewer, *J. Am. Chem. Soc.* **2022**, *144*, 13205–13217.

[12] A. Zagalskaya, I. Evazzade, V. Alexandrov, *ACS Energy Lett.* **2021**, *6*, 1124–1133.

[13] a) Y. E. Roginskaya, T. V. Varlamova, M. D. Goldstein, I. D. Belova, B. S. Galyamov, R. R. Shifrina, V. A. Shepelin, V. N. Fateev, *Mater. Chem. Phys.* **1991**, *30*, 101–113; b) Y. Murakami, K. Miwa, M. Ueno, M. Ito, K. Yahikozawa, Y. Takasu, *J. Electrochem. Soc.* **2019**, *141*, L118–L120.

[14] I. C. Man, PhD thesis, Technical University of Denmark (DK) **2011**.

[15] A. H. Reksten, H. Thuv, F. Seland, S. Sunde, *J. Electroanal. Chem.* **2018**, *819*, 547–561.

[16] a) A. T. Marshall, L. Vaisson-Béthune, *Electrochem. Commun.* **2015**, *61*, 23–26; b) A. T. Marshall, A. Herritsch, *ECS Trans.* **2018**, *85*, 121–130.

[17] a) U. Krewer, M. Christov, T. Vidaković, K. Sundmacher, *J. Electroanal. Chem.* **2006**, *589*, 148–159; b) U. Krewer, T. Vidaković-Koch, L. Rihko-Struckmann, *ChemPhysChem* **2011**, *12*, 2518–2544.

[18] a) J. Geppert, F. Kubannek, P. Röse, U. Krewer, *Electrochim. Acta* **2021**, *380*, 137902; b) T. Haisch, F. Kubannek, L. Nikitina, I. Nikitin, S. Pott, T. Clees, U. Krewer, *Phys. Chem. Chem. Phys.* **2020**, *22*, 16648–16654; c) P. Schön, U. Krewer, *Electrochim. Acta* **2021**, *373*, 137523.

[19] V. A. Saveleva, L. Wang, W. Luo, S. Zafeiratos, C. Ulhaq-Bouillet, A. S. Gago, K. A. Friedrich, E. R. Savinova, *J. Phys. Chem. Lett.* **2016**, *7*, 3240–3245.

[20] C. F. Dickens, C. Kirk, J. K. Nørskov, *J. Phys. Chem. C* **2019**, *123*, 18960–18977.

[21] L. G. V. Briquet, M. Sarwar, J. Mugo, G. Jones, F. Calle-Vallejo, *ChemCatChem* **2017**, *9*, 1261–1268.

[22] Z. Ma, Y. Zhang, S. Liu, W. Xu, L. Wu, Y.-C. Hsieh, P. Liu, Y. Zhu, K. Sasaki, J. N. Renner, K. E. Ayers, R. R. Adzic, J. X. Wang, *J. Electroanal. Chem.* **2018**, *819*, 296–305.

[23] T. Ikeshoji, M. Otani, *Phys. Chem. Chem. Phys.* **2017**, *19*, 4447–4453.

[24] a) R. Afonso, L. Gales, A. Mendes, *Adsorption* **2016**, *22*, 963–971; b) J. H. de Boer, *The dynamical character of adsorption*, Clarendon Press, London **1953**.

[25] a) S. R. Cole, H. Chu, S. Greenland, *Am. J. Epidemiol.* **2014**, *179*, 252–260; b) A. Raue, C. Kreutz, T. Maiwald, J. Bachmann, M. Schilling, U. Klingmuller, J. Timmer, *Bioinformatics* **2009**, *25*, 1923–1929.